Performance Bound Analysis of Analog Circuits in Frequency- and Time-Domain Considering Process Variations

XUE-XIN LIU and SHELDON X.-D. TAN, University of California, Riverside
ADOLFO ADAIR PALMA-RODRIGUEZ and ESTEBAN TLELO-CUAUTLE, National Institute of Astrophysics, Optics, and Electronics (INAOE)
GUOYONG SHI, Shanghai Jiao Tong University

In this article, we propose a new performance bound analysis of analog circuits considering process variations. We model the variations of component values as intervals measured from tested chips and manufacture processes. The new method first applies a graph-based analysis approach to generate the symbolic transfer function of a linear(ized) analog circuit. Then the frequency response bounds (maximum and minimum) are obtained by performing nonlinear constrained optimization in which magnitude or phase of the transfer function is the objective function to be optimized subject to the ranges of process variational parameters. The response bounds given by the optimization-based method are very accurate and do not have the over-conservativeness issues of existing methods. Based on the frequency-domain bounds, we further develop a method to calculate the time-domain response bounds for any arbitrary input stimulus. Experimental results from several analog benchmark circuits show that the proposed method gives the correct bounds verified by Monte Carlo analysis while it delivers one order of magnitude speedup over Monte Carlo for both frequency-domain and time-domain bound analyses. We also show analog circuit yield analysis as an application of the frequency-domain variational bound analysis.

Categories and Subject Descriptors: J.6 [**Computer Application**]: Computer-Aided Engineering— *Computer-aided design (CAD)*

General Terms: Design, Algorithms

Additional Key Words and Phrases: Circuit simulation, worst-case analysis, bound analysis, process variation

1. INTRODUCTION

It is well accepted that variations have huge impacts on circuit performance, yield, and reliability in the nanometer regime. Analog and mixed-signal circuits are especially sensitive to process variations, as a lot of matching and regularities are required. This situation becomes worse as technology continues to scale down to 45 nm and below, owing to the increasing process-induced variability [Rutenbar 2007; Nassif 2007]. Transistor-level mismatch is the primary obstacle to reaching a high yield rate for analog designs in deep submicron technologies. For example, due to an

inverse-square-root-law dependence with the transistor area, the mismatch of CMOS devices nearly doubles for each process generation less than 90 nm [Masuda et al. 2005; Kim et al. 2007]. Since the traditional worst-case- or corner-case-based analysis is either so pessimistic that it sacrifices speed, power, and area, or too expensive for practical full-chip design, statistical approaches thereby become imperative to estimate the analog mismatch and performance variations [Pelgrom et al. 1989]. The variations in the analog components can come from systematic (or global spatial variation) ones and stochastic (or local random variation) ones. In this article, we model both variations as parameter intervals on the components of analog circuits.

Analog circuit designers usually perform a Monte-Carlo (MC) analysis to analyze the stochastic mismatch and predict the variational responses of their designs under faults. As MC analysis requires a large number of repeated circuit simulations, its computational cost is very expensive. Although some fast MC methods have been applied for statistical and yield analysis recently [Singhee and Rutenbar 2010; Liu et al. 2012], we remark that MC and its variants still remain the popular approaches for statistical analysis and optimization for analog/mixed-signal methods at current stage. But more efficient variational analysis techniques, especially non-MC methods, are still highly desirable. Our work takes some initiative efforts toward this direction. We do not aim to solve all the existing problems. Instead, we try to look at the basic problem for statistical analysis—finding the performance bounds of linear or linearized analog circuits for given variational parameters—which will lay the foundation for future performance bound analysis for general nonlinear analog/mixed-signal circuits.

Bound analysis or worst-case analysis of analog circuits under parameter variations has been studied in the past for fault-driven testing and tolerance analysis of analog circuits [Kolev et al. 1988; Tian et al. 1996; Shi and Tian 1999]. Among them, sensitivity analysis [Vlach and Singhal 1995], sampling method [Spence and Soin 1988], and interval arithmetic-based approaches [Kolev et al. 1988; Tian et al. 1996; Shi and Tian 1999; Qian et al. 2010] have their advantages in well-suited scenarios. However, sensitivity-based methods cannot give the worst case in general; sampling-based methods are limited to a few number variables; and interval arithmetic methods have the notoriety of being overly pessimistic. Recently, worst-case analysis of linearized analog circuits in frequency domain has been proposed [Qian et al. 2010], where Kharitonov's functions [Kharitonov 1978] were applied to obtain the performance bounds in frequency domain, but no systematic method was proposed to obtain variational transfer functions. This was later improved by Hao et al. [2011], where symbolic analysis approach was applied to derive exact transfer functions, and affine interval method was used to compute variational transfer functions. However, the affine interval method can lead to over-conservative results. Recently, Saibua et al. [2011] applied an optimization-based method to compute the bounds. Another recent work [Song et al. 2013], using reachability analysis, can also efficiently generate variation-induced performance bounds. But still, no systematic method has been proposed to obtain variational performance objective functions from the circuit netlist.

In this article, we propose a new performance bound analysis of analog circuits considering process variations. The new method employs several techniques to compute the response bounds of analog circuits in both frequency domain and time domain. The overall algorithm consists of several steps. First, the new method models the variations of component values as intervals measured from tested chips and manufacture processes. Then, determinant decision diagram (DDD) graph-based symbolic analysis is applied to derive the exact symbolic transfer functions from linearized analog circuits. After this, we formulate the bound problem into a nonlinear constrained optimization problem, where the objective functions are the magnitudes or phases of the transfer functions, subject to linear constraints, which are the ranges of process
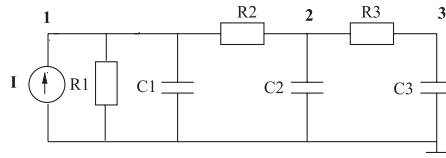
Fig. 1.   An RC filter circuit.

variational parameters. The nonlinear constrained optimization problems are then solved by the active-set algorithm, a general nonlinear optimization method. The optimization is solved on each frequency point of interest. The maximum and minimum value returned by the optimization solver will compose the lower and upper bounds of the frequency-domain response. One important feature of the proposed method is that the bounds computed in this way are very accurate and have no over-conservativeness, which is suffered by some existing approache, such as interval arithmetic or affine arithmetic-based methods. As an application of our frequency-domain bound analysis, we also show results of analog circuit yield calculation in the experiment section.

To compute the time-domain bound, we propose a generalized time-domain bound analysis technique, or TIDBA, in which time-domain response bounds of circuits with general input signals can be computed based on the given frequency-domain responses. This represents a major improvement over the existing method [Pritchard and Wigdorowitz 1997]. Experimental results from several analog benchmark circuits show that TIDBA gives the correct time-domain bounds verified by MC analysis, while it delivers one order of magnitude speedup over MC.

The rest of this article is organized as follows. Section 2 gives a review on determinant decision diagram-based symbolic generation of transfer functions. We present our proposed frequency domain performance-bound analysis using nonlinear constrained optimization in Section 3. Then Section 4 introduces time-domain bound analysis TIDBA. Section 5 shows the experimental results. Finally, Section 6 concludes.

2. DETERMINANT DECISION DIAGRAMS AND VARIATIONAL TRANSFER FUNCTIONS

In this section, we first provide a brief overview of the determinant decision diagram (DDD) [Shi and Tan 2000] and its application to symbolic analysis. Then we show the concept of variational transfer functions.

2.1. Symbolic Transfer Functions by DDD-Based Approaches

To efficiently store and calculate determinants of circuit matrices and transfer functions, Shi and Tan [2000] introduced *determinant decision diagrams* as compact and canonical graph-based representation of determinants. The concept is best illustrated using the simple RC filter circuit shown in Figure 1. Its MNA formulation can be written as $\mathbf{Y} \cdot \mathbf{v} = \mathbf{i}$, where $\mathbf{Y}$ is the MNA matrix

$$\begin{bmatrix} \frac{1}{R_1} + sC_1 + \frac{1}{R_2} & -\frac{1}{R_2} & 0 \\ -\frac{1}{R_2} & \frac{1}{R_2} + sC_2 + \frac{1}{R_3} & -\frac{1}{R_3} \\ 0 & -\frac{1}{R_3} & \frac{1}{R_3} + sC_3 \end{bmatrix},$$

vector $\mathbf{i} = [I(s), 0, 0]^{\mathrm{T}}$ is the right-hand side vector of current stimulus, and the vector of nodal voltages to be solved is $\mathbf{v} = [v_1(s), v_2(s), v_3(s)]^{\mathrm{T}}$.

We view each entry in the circuit matrix as a distinct symbol and rewrite its system determinant in the left part of Figure 2. Then its DDD representation is shown in the right part.
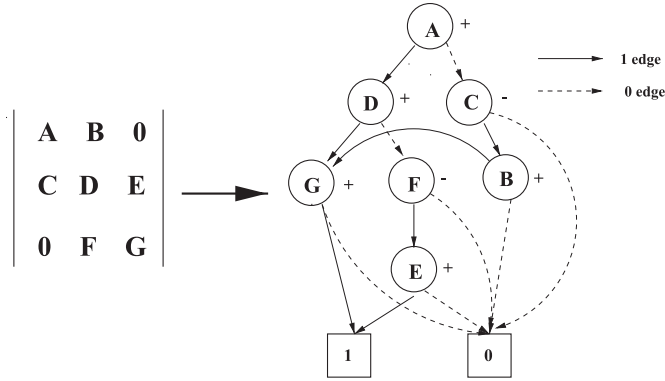
Fig. 2. A matrix determinant and its DDD representation.

A DDD is a signed, rooted, directed acyclic graph with two terminal vertices, namely, 0-*terminal* vertex and 1-*terminal* vertex. Each nonterminal DDD vertex is labeled by a symbol in the determinant denoted by a_i (A to G in Figure 2), and a positive or negative sign denoted by $s(a_i)$. It originates two outgoing edges, called 1-*edge* and 0-*edge*. Each vertex a_i represents a symbolic expression $D(a_i)$ defined recursively as follows:

$$D(a_i) = a_i \cdot s(a_i) \cdot D_{a_i} + D_{\bar{a}_i}, \tag{1}$$

where D_{a_i} and $D_{\bar{a}_i}$ represent, respectively, the symbolic expressions of the vertices pointed by the 1-edge and 0-edge of a_i. The 1-terminal vertex represents expression 1, whereas the 0-terminal vertex represents expression 0. For example, vertex E in Figure 2 represents expression E, vertex F represents expression $-EF$, and vertex D represents expression $DG - FE$. We also say that a DDD vertex represents an expression defined by the DDD subgraph rooted at this vertex.

A 1-*path* in a DDD corresponds with a product term in the original DDD, which is defined as a path from the root vertex (A in our example) to the 1-terminal, including all symbolic symbols and signs of the vertices that originate all the 1-edges along the 1-path. In our example, there exist three 1-paths representing three product terms: ADG, $-AFE$, and $-CBG$. The root vertex represents the sum of these product terms. The size of a DDD is the number of DDD vertices, denoted by |DDD|.

Once a DDD has been constructed, the numerical values of the determinant it represents can be computed by performing the depth-first type search of the graph and evaluating Eq. (1) at each node, whose time complexity is a linear function of the size of the graphs, that is, |DDD|. With proper node ordering and hierarchical approaches, DDD can be very efficient in computing transfer functions of large analog circuits [Shi and Tan 2000; Tan et al. 2005].

2.2. Variational Transfer Functions Due to Process Variations

In order to compute the symbolic coefficients of the transfer function in different powers of frequency s, the original DDD can be expanded to the s-expanded DDD [Shi and Tan 2001]. Specifically, to obtain the transfer function $H(s)$, we can build the s-expanded DDD [Shi and Tan 2001] as follows.

$$H(s, p_1, \ldots, p_m) = \frac{\sum_{i=0}^m a_i(p_1, \ldots, p_m)s^i}{\sum_{j=0}^n b_j(p_1, \ldots, p_m)s^j}, \tag{2}$$
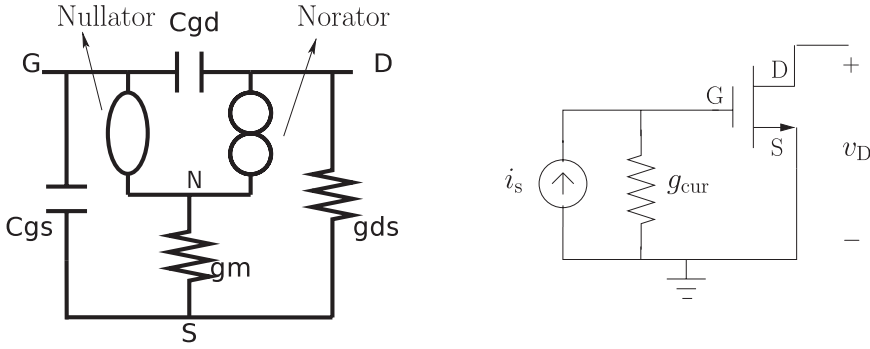
Fig. 3.   The small-signal model for MOS transistors (left) and a simple circuit example (right).

where coefficients $a_i(p_1, \ldots, p_m)$ and $b_j(p_1, \ldots, p_m)$ are presented by each root in s-expanded DDD graphs, and $p_1, \ldots, p_m$ are m circuit variables. Notice that $H(s, p_1, \ldots, p_m)$ is a nonlinear function of $p_i, i = 1, \ldots, m$.

In this article, we assume that each circuit parameter p_i is a random variable with a variational range. We assume that the device-level variations in terms of electrical parameters, such as transconductances g_m and g_{ds} (shown in Figure 3), will be first obtained by device characterization using data from the foundry. Let $s = j\omega$. The evaluation of the transfer function gives a complex valued result, $H(j\omega) = H^0(\omega)e^{j\theta(\omega)}$, where the magnitude $H^0(\omega) = |H(j\omega)|$ and the phase angle $\theta(\omega) = \angle H(j\omega)$ are real values. In variation analysis, instead of getting a nominal transfer function, we will obtain a variational transfer function with bounded magnitude and phase regions, that is,

$$H_l^0(\omega) \leq H^0(\omega) \leq H_u^0(\omega), \tag{3}$$

$$\theta_l(\omega) \leq \theta(\omega) \leq \theta_u(\omega), \tag{4}$$

where $H_l^0(\omega)$ and $H_u^0(\omega)$ are the lower and upper bounds of magnitude, and $\theta_l(\omega)$ and $\theta_u(\omega)$ are the lower and upper bounds of phase.

3. COMPUTATION OF FREQUENCY DOMAIN BOUNDS

In this section, we first describe the performance bounds in frequency domain for a circuit under process variation. Then, to compute the bounds, we propose the optimization-based method, which is very general and accurate.

We start with a specific example to look at the frequency-domain bound problem. The example is a simplified MOS device model, as shown in the left part of Figure 3, in which the singular network elements, like nullator and norators, are used to model the ideal voltage-controlled current sources (VCCS). Suppose we apply a Norton current source, that is, an ideal current source i_s with a parallel resistor g_{cur}, shown in the right part of Figure 3, onto the gate node G of the MOS model, the exact symbolic transfer function from i_s to the observed voltage on drain node D can be obtained as

$$H(j\omega) = \frac{v_D(j\omega)}{i_s(j\omega)} = \frac{g_m - j\omega C_{gd}}{(j\omega)^2 C_{gs}C_{gd} + j\omega(C_{gs}g_{ds} + C_{gd}(g_{ds} + g_m + g_{cur})) + g_{ds}g_{cur}}. \tag{5}$$

Once the exact transfer function and variations of the parameters, such as g_m, g_{ds}, C_{gd}, and C_{gs}, are known, one can find the bounds of $H(j\omega)$. The variational bounds of the transfer function are plotted in Figure 4, where we have two variational parameters g_{ds} and g_m. The variation spaces for the two variables at three different frequencies are also shown on the top of the figure, which show the searching spaces at those frequencies
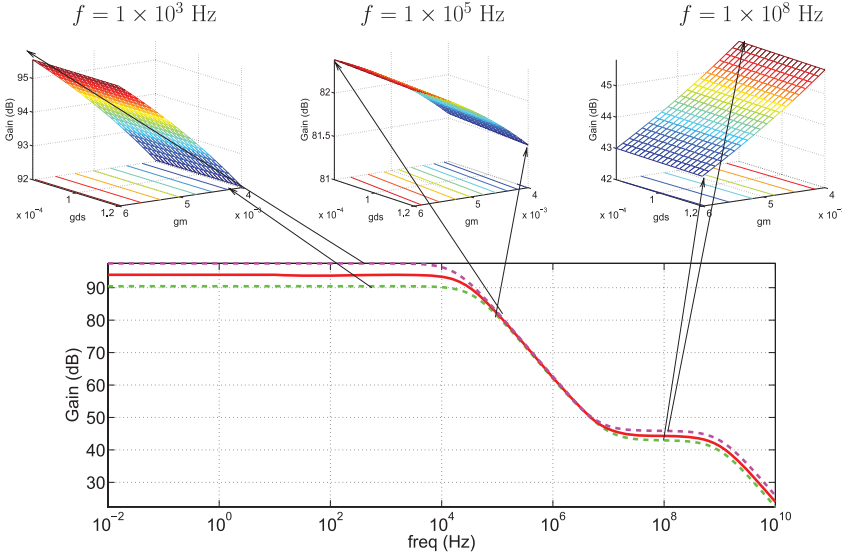
Fig. 4.   Frequency response of the simplified MOS model driven by Norton current source. The solid curve is the magnitude response with nominal parameters, while the two dashed curves are lower and upper bounds due to process variation. The three surfaces on top, with g_{ds} and g_{m} as the x-axis and y-axis accordingly, and magnitude as z-axis, illustrate the variations of magnitude at three sampling frequencies.

for the two variables. Here, we adopt the term *searching spaces* from mathematical programming and optimization, which is used in our proposed method and will be talked about later.

To obtain the performance bounds of analog circuits in the frequency domain, the first step is to obtain the exact symbolic transfer functions, like Eq. (5), in terms of all the variational circuit parameters. This will be done by the DDD-based exact symbolic analysis, as mentioned in Section 2. We remark that one can also use a circuit simulator, like SPICE, to evaluate the performances for a given set of parameter values and frequency points. But the DDD method is relevant here because it can give closed-form expressions for a given circuit performance, which can lead to much faster evaluations compared to numerical methods [Shi and Tan 2000].

Second, after the exact symbolic transfer functions are available, we need to find a systematic way to obtain the performance bounds given the bounds of variational parameters. In this work, we formulate the bound computing problem into a nonlinear constrained optimization problem. To obtain the performance bounds for magnitude and phase at one frequency point, four evaluation processes, or optimization runs, of the transfer function are needed: min/max optimizations for $H^0(\omega)$ and min/max optimizations for $\theta(\omega)$. The range of frequency sweep and number of frequency points are determined freely by the designer. We use the lower bound of the magnitude response $H^0(\omega)$ for an example. The magnitude of the transfer function, which can be evaluated from the available symbolic transfer function, is used as the nonlinear objective function to be minimized:

$$\begin{aligned} \text{minimize} \quad & H^0(\omega, \mathbf{x}) \\ \text{subject to} \quad & \mathbf{x}_{\text{lower}} \le \mathbf{x} \le \mathbf{x}_{\text{upper}}, \end{aligned} \tag{6}$$

where $\mathbf{x} = [p_1, \ldots, p_m]$ represents the circuit parameter variable vector, which is subject to the optimization constraints $\mathbf{x}_{\text{lower}} \le \mathbf{x} \le \mathbf{x}_{\text{upper}}$. In circuit design, these constraints
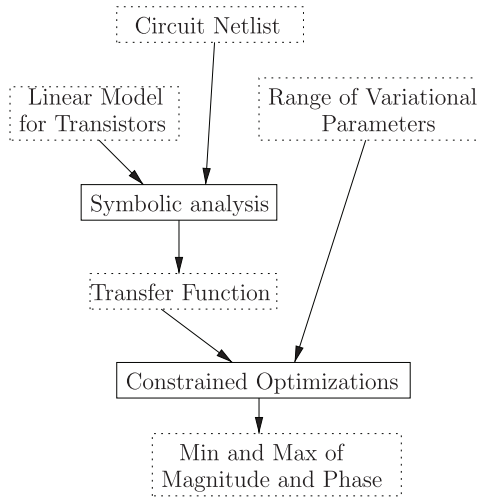
Fig. 5.   The flowchart of frequency domain performance bound calculation.

are supplied by foundries and cell library vendors. Hence, after Eq. (6) is solved by an optimization engine, the lower bound of the magnitude response at ω, that is, $H_l^0(\omega)$, is returned, and a parameter set $\mathbf{x}^*$ at which the minimum is attained will also be saved as a by-product.

We remark that the worst cases of magnitude may not be the worst cases of phase, and the two worst-case performance metrics do not have specific correlations. After we calculate the worst case for the performances of interests, such as magnitude or phase, at every frequency point, we can obtain the worst-case curves (upper or lower bounds) in the frequency domain, as shown in Figure 4.

The nonlinear optimization problem with simple upper and lower bounds given in Eq. (6) can be efficiently solved by several methods, such as active-set, interior point, and trust region algorithms [Byrd et al. 1987; Gill et al. 1997; Floudas 1995]. All these methods are iterative approaches starting with an initial feasible solution. In this work, we use the active-set method [Floudas 1995], as it turns out to be the most robust nonlinear optimization method for our application. Active-set methods are two-phase iterative methods that provide an estimate of the active set (*active set* is the set of constraints that are satisfied with equality) at the solution. In the first phase, the objective is ignored, while a feasible point $\mathbf{x}_0$ is found for the constraints. In the second phase, the objective is minimized while feasibility is maintained. Starting from the feasible $\mathbf{x}_0$, the second phase computes a sequence of feasible solutions $\{\mathbf{x}_k\}$ such that $\mathbf{x}_{k+1} = \mathbf{x}_k + \alpha_k \mathbf{p}_k$, where $\mathbf{p}_k$ is a nonzero search direction and α_k is a nonnegative step length. Hence, the new solution $\mathbf{x}_{k+1}$ makes the cost function or objective function smaller than its precedent $\mathbf{x}_k$ does. Methods like quadratic programming can be used in this phase.

To further speed up the optimization, the initial point selection can be further improved. Since the responses at two neighboring frequency points are usually close to each other, the starting point $\mathbf{x}$ for frequency point ω_{i+1} can be set using the solution at the previous frequency point ω_i. Therefore, the initial guess point does not always have to be the nominal value set, and the previous frequency's optimal point is heuristically the best shortcut of initial guess at current frequency. This strategy tends to reduce the time required by the optimization to search its minimal or maximal point in

ALGORITHM 1: Calculation of Frequency Response Bounds via Symbolic Analysis and Non-linear Constrained Optimization

---

1: Read circuit netlist.
2: Set bounds on process variation affected parameters.
3: Generate symbolic expression of transfer functions.
4: **for** each frequency ω_i **do**
5:     Nonlinear constrained optimization (6) which uses transfer function as objective to find magnitude and phase bounds on ω_i.
6: **end for**
7: Save bound information for future statistical and yield analysis.

---

the whole variation space, and thus speed up the calculation time of the bound analysis. Figure 5 summarizes the flow of the performance bound calculation.

We remark that the active-set method is still a local optimization method, which finds the local optimum. It will be desirable to find the global optimum, which can give true "confident" bounds of performance. But this goal may come with more or much higher computing costs by performing many tries. The effort boils down to a trade-off between accuracy and costs in this problem. In our approach, we still perform one optimization. Our experimental results show that by using reasonable initial guesses, as mentioned before, the proposed method gives very close bounds compared with MC methods for the examples being used.

4. TIME-DOMAIN BOUND ANALYSIS METHOD

In the previous section, we have shown our frequency-domain performance bound method using symbolic analysis and constrained optimization. Based on the calculated frequency-domain bounds, we next develop our time-domain bound analysis, or TIDBA, which converts the frequency-domain bounds to time-domain bounds for general input signals. TIDBA is inspired by Pritchard and Wigdorowitz [1997], which determines time-domain performance bounds of an uncertain system for impulse or step input signals. However, this method does not give transient performance bounds in response to general input signals, which are required by analog circuit analysis. Note that the bounds of magnitude and phase of the transfer function required by TIDBA can be generated by any existing bound analysis methods and not limited to the one we proposed in the previous section.

We first present the whole TIDBA flow in Algorithm 2. As can be seen from the flow, the time-domain bound analysis requires the results, such as transfer function bounds from the procedures we studied in previous sections. After the first two steps, the bounds of magnitude and phase (angle) shown in Inequalities (3) and (4) are available. Then TIDBA converts frequency-domain performance bounds into time-domain performance bounds by impulse-signal-based time-domain bound analysis and FFT/IFFT, which will be the focus of this section.

4.1. Review of Transient Bound Analysis Driven by Impulse Signals

For the completeness of our presentation, we briefly review the work in Pritchard and Wigdorowitz [1997], which provides transient bound analysis with impulse input signals.

For a purely real signal $x(t)$ in the time domain, its Fourier transform $X(j\omega) = X^0(\omega) \cdot e^{j\phi(\omega)}$ in the frequency domain holds the property of conjugate symmetry, that is,

$$X(-j\omega) = X(j\omega)^*. \tag{7}$$

ALGORITHM 2: The Algorithm Flow of the New Time-Domain Performance Bound Analysis—TIDBA

Input: Circuit netlist with variational parameters; stimulus signal of the circuit.
Output: Lower and upper bounds of the output signal in time domain.
  1: Generate symbolic expression of circuit transfer function by graph-based symbolic method. Variational parameters are represented as symbols.
  2: Compute the performance bounds of the variational transfer function by nonlinear constrained optimization.
  3: Compute time domain performance bounds by our new general-signal transient bound analysis presented in Section 4.2.

It can be equivalently expressed by the even property of magnitude and the odd property of phase: $X^0(-\omega) = X^0(\omega)$, and $\phi(-\omega) = -\phi(\omega)$. It is not difficult to show that the transfer function of a physically-realizable system also holds the conjugate symmetry property [Lathi 1998].

Since the spectrum of an impulse signal $\delta(t)$ is $X(j\omega) = 1$ everywhere on all frequencies, the spectrum of the system's output signal is $Y(j\omega) = X(j\omega)H(j\omega) = H(j\omega)$, and hence the impulse response of the system in time domain is simply the inverse Fourier transform of $H(j\omega)$,

$$
\begin{aligned}
y(t) &= \frac{1}{2\pi} \int_{-\infty}^{\infty} H(j\omega)e^{j\omega t}\, \mathrm{d}\omega \\
&= \frac{1}{2\pi} \int_{-\infty}^{\infty} H^0(\omega)e^{j(\omega t + \theta(\omega))}\, \mathrm{d}\omega, \quad t > 0.
\end{aligned}
\tag{8}
$$

Employing the even and odd properties of $H(j\omega)$, Eq. (8) can be equivalently integrated from $\omega = 0$ to ∞,

$$
\begin{aligned}
y(t) &= \frac{1}{\pi} \int_{0}^{\infty} H^0(\omega)\mathrm{Re}\big(e^{j(\omega t + \theta(\omega))}\big)\, \mathrm{d}\omega \\
&= \frac{1}{\pi} \int_{0}^{\infty} H^0(\omega)\cos(\omega t + \theta(\omega))\, \mathrm{d}\omega, \quad t > 0.
\end{aligned}
\tag{9}
$$

A modification of this integral to discrete sum on sampled frequency points allows one to calculate the approximate result of $y(t)$ at each time point as

$$
y(t) = \frac{1}{\pi} \sum_{n=0}^{N-1} \underbrace{H^0(\omega_n)\cos(\omega_n t + \theta(\omega_n))}_{I(\omega_n)} \Delta\omega_n, \quad t > 0.
\tag{10}
$$

In the presence of process variation, the transfer function will be given in the bounded form in Inequalities (3) and (4). Therefore, to compute the lower and upper transient bounds $y_l(t)$ and $y_u(t)$ for each time point t, the integrand body $I(\omega_n)$ in Eq. (10) is calculated using the following rules.

First, find the minimum and maximum values of $\cos(\omega_n t + \theta(\omega_n))$, where the phase angle $\theta(\omega_n)$ can vary in the interval $[\theta_l(\omega_n), \theta_u(\omega_n)]$. Let $C_{\min}(\omega_n)$ and $C_{\max}(\omega_n)$ denote the two extreme values of the cosine function. Then, for $y_l(t)$, all $I(\omega_n)$ shall be calculated as

$$
I(\omega_n) = \begin{cases} H_u^0(\omega_n)C_{\min}(\omega_n), & C_{\min}(\omega_n) \le 0 \\ H_l^0(\omega_n)C_{\min}(\omega_n), & C_{\min}(\omega_n) > 0, \end{cases}
\tag{11}
$$

and, for $y_u(t)$, the situation is simply reversed,

$$I(\omega_n) = \begin{cases} H_l^0(\omega_n)C_{max}(\omega_n), & C_{max}(\omega_n) \leq 0 \\ H_u^0(\omega_n)C_{max}(\omega_n), & C_{max}(\omega_n) > 0. \end{cases} \tag{12}$$

4.2. Proposed General Signal Transient Bound Analysis Method

For a general time-domain signal $x(t)$ in circuit analysis application, its frequency-domain transform $X(j\omega)$ can be calculated by fast Fourier transform, FFT. This requires sampling points of the signal on a set of discretized time points. For example, with a uniform sampling period $T_s = 1/F_s$, $x(t)$ is sampled and stored as $x(0), x(T_s), x(2T_s), \ldots,$ $x(NT_s)$. For the sake of simplicity, we will omit the term T_s and denote the time point indices by subscripts in the remainder of this paper. Thus the notation x_n will stand for the sampled value of signal $x(t)$ at time $t = nT_s$.

To achieve accurate results from FFT and IFFT, the Nyquist sampling theorem requires the sampling frequency $F_s = 1/T_s$ to be at least twice that of the bandwidth of the signal [Oppenheim and Schafer 1999]. Meanwhile, the total sampling duration $T_0 = T_s N$ determines the resolution of the FFT spectrum, that is, the sampling interval of frequency domain is $F_0 = 1/T_0$. The longer T_0 is, the higher spectral resolution we can get, and thus the more sampling points are needed.

Given N sampling points, the FFT transform pair is

$$X_k = \sum_{n=0}^{N-1} x_n e^{-j\frac{2\pi}{N}nk}, \quad k = 0, 1, \ldots, N-1, \text{ and} \tag{13}$$

$$x_n = \frac{1}{N} \sum_{k=0}^{N-1} X_k e^{j\frac{2\pi}{N}nk}, \quad n = 0, 1, \ldots, N-1. \tag{14}$$

In transient circuit analysis, the input data x_n are purely real, and the symmetry property in Eq. 7 still holds, though in a different form, $X_{N-k} = X_k^*$. This means that the right half of spectrum X_k is a conjugate swap of its left half, except for X_0, which is the zero-frequency or "DC" component of the spectrum. The points in the left half, that is, X_k for $k = 0, \ldots, N/2$, are the spectral points of frequencies $f = kF_0$. Figure 6 illustrates the FFT series and its conjugate symmetry property.

Based on this property of a real signal's spectrum, the inverse discrete Fourier transform can be calculated with the spectrum's left half. Consequently, the equivalent form of Eq. (14) becomes

$$x_n = \frac{1}{N} \left[X_0 + 2 \sum_{k=1}^{N/2} \text{Re}\left(X_k e^{j\frac{2\pi}{N}nk}\right) \right], \quad n = 0, 1, \ldots, N-1. \tag{15}$$

We remark that using only the left half of the complex-valued frequency-domain samplings is not just for the sake of simplifying the text. In implementation, this also saves processing time and storage memory. The popular FFT library FFTW now provides a function interface for this so-called *halfcomplex* application. Further details about its usage in our program can be found at in Frigo and Johnson [2013].

Now it is the time to derive the time response bounds from the FFT series of signal $x(t)$ given the frequency response bounds of the system $H(j\omega)$. First we consider the system without variation. After FFT is applied to x_n, as represented in Eq. (13), its spectrum $X_k = |X_k|e^{j\phi_k}$ is multiplied with $H_k = H(j\omega_k)$, $\omega_k = 2\pi kF_0$, to obtain the spectrum of output signal. Then, we make a domain translation from the frequency domain to time domain, which is similar to Eq. (15). In this way, the output signal y_n
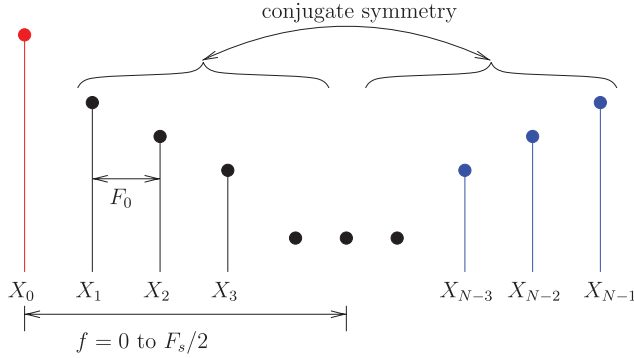
Fig. 6. Conjugate symmetry between left half and right half of the FFT series X_k, $k = 0, \ldots, N-1$.

is obtained for the nominal designed system.

$$y_n = \frac{1}{N}\left[Y_0 + 2\sum_{k=1}^{N/2}\mathrm{Re}\big[Y_k e^{j\frac{2\pi}{N}nk}\big]\right]$$

$$= \frac{1}{N}\left[X_0 H^0(0) + 2\sum_{k=1}^{N/2}\mathrm{Re}\big[H^0(\omega_k)e^{j\theta(\omega_k)}X_k e^{j\frac{2\pi}{N}nk}\big]\right]$$

$$= \frac{1}{N}\left[X_0 H^0(0) + 2\sum_{k=1}^{N/2}|X_k|H^0(\omega_k)\mathrm{Re}\big[e^{j(\phi_k+\theta(\omega_k)+\frac{2\pi}{N}nk)}\big]\right]. \quad (16)$$

Now we consider the process variations. In this case, the minimum and maximum values, similar to Eqs. (11) and (12) for impulse signals, have to be derived from Eq. (16) in the bounded region of the system transfer function at every frequency point. Specifically, the selection and combinations of $H^0(\omega)$ and $\theta(\omega)$ will depend on the sign of the real part of the output spectrum, that is, $\mathrm{Re}\{e^{j(\phi_k+\theta(\omega_k)+\frac{2\pi}{N}nk)}\}$. Detailed analysis shows that there are many combinations of extreme values of $H^0(\omega)$ and $\theta(\omega)$, depending on the locations of $\phi_k + \theta(\omega_k) + \frac{2\pi}{N}nk$ in the complex plane, which are summarized in Table I. Let's walk through one example illustrated in Figure 7, where all possible values of $\theta(\omega_k)$ make the phase $\phi_k + \theta(\omega_k) + \frac{2\pi}{N}nk$ fall in the first quadrant, and thus their real parts are all positive. Therefore, the selection of $H_l^0(\omega_k)$ and $\theta_u(\omega_k)$ will lead to the minimum of output value, while $H_u^0(\omega_k)$ and $\theta_l(\omega_k)$ lead to the maximum one. In Figure 7, these two combinations are marked by black dots.

We remark that the range of allowed phase values $[\theta_l(\omega_k), \theta_u(\omega_k)]$ affects the rules for bound determination, as shown in Table I. In this article, we restrict the maximum phase range to be less than 90 degrees, that is, $\theta_u(\omega_k) - \theta_l(\omega_k) < \pi/2$ rads. There are two reasons for this restriction: (1) the restriction of 90 degrees accommodates most circuit transfer function's variation very well; (2) if much larger phase variation is detected at the frequency domain, the variation will likely cause faults in the circuit. We stress that there is no difficulty in generating new bound determination rules to handle phase ranges larger than 90 degrees.

With this assumption, the rules for time-domain bound determination are summarized in Table I. For brevity, let $\Theta_l(\omega_k) = \phi_k + \theta_l(\omega_k) + \frac{2\pi}{N}nk$, and $\Theta_u(\omega_k) = \phi_k + \theta_u(\omega_k) + \frac{2\pi}{N}nk$. If the range of Θ is not covered by the enumerated regions, a phase shift of 2π could be applied to relocate its value into the listed ranges. In addition, the "either
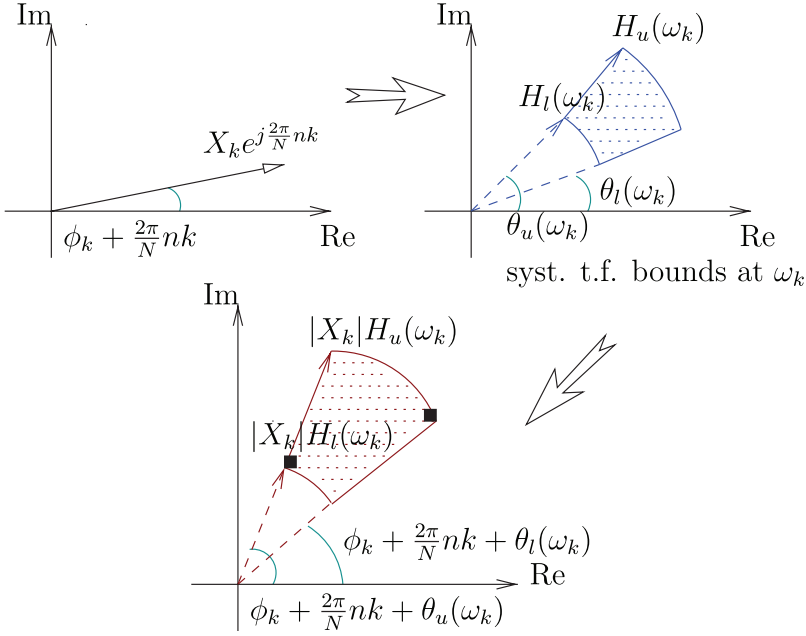
Fig. 7. The magnification and rotation of input spectrum by the transfer function bounds.

Table I. Rules for Time-Domain Bound Determination

range of phase		quad-	sign of	magnitude and phase combinations for			
$\Theta_l(\omega_k)$	$\Theta_u(\omega_k)$	rants	$\mathrm{Re}[e^{j\Theta}]$	lower bound		upper bound	
$(-\pi/2, 0)$	$(0, \pi/2)$	IV, I	$+$	$H_l^0(\omega_k)$	either $\Theta_l(\omega_k)$ or $\Theta_u(\omega_k)$	$H_u^0(\omega_k)$	$\Theta(\omega_k) = 0$
$(0, \pi/2)$	$(0, \pi/2)$	I	$+$	$H_l^0(\omega_k)$	$\Theta_u(\omega_k)$	$H_u^0(\omega_k)$	$\Theta_l(\omega_k)$
$(0, \pi/2)$	$(\pi/2, \pi)$	I, II	$+, -$	$H_u^0(\omega_k)$	$\Theta_u(\omega_k)$	$H_u^0(\omega_k)$	$\Theta_l(\omega_k)$
$(\pi/2, \pi)$	$(\pi/2, \pi)$	II	$-$	$H_u^0(\omega_k)$	$\Theta_u(\omega_k)$	$H_l^0(\omega_k)$	$\Theta_l(\omega_k)$
$(\pi/2, \pi)$	$(\pi, 3\pi/2)$	II, III	$-$	$H_u^0(\omega_k)$	$\Theta(\omega_k) = \pi$	$H_l^0(\omega_k)$	either $\Theta_l(\omega_k)$ or $\Theta_u(\omega_k)$
$(\pi, 3\pi/2)$	$(\pi, 3\pi/2)$	III	$-$	$H_u^0(\omega_k)$	$\Theta_l(\omega_k)$	$H_l^0(\omega_k)$	$\Theta_u(\omega_k)$
$(\pi, 3\pi/2)$	$(3\pi/2, 2\pi)$	III, IV	$+, -$	$H_u^0(\omega_k)$	$\Theta_l(\omega_k)$	$H_u^0(\omega_k)$	$\Theta_u(\omega_k)$
$(3\pi/2, 2\pi)$	$(3\pi/2, 2\pi)$	IV	$+$	$H_l^0(\omega_k)$	$\Theta_l(\omega_k)$	$H_u^0(\omega_k)$	$\Theta_u(\omega_k)$

$\Theta_l(\omega_k)$ or $\Theta_u(\omega_k)$" in the first row and the fifth row in the table means one of them will be selected: in the first row, the lower bound will happen at one of them, which makes $\cos(\Theta)$ smaller; and in the fifth row, the upper bound will take place at the phase angle making $\cos(\Theta)$ larger. Similarly, the uncertainty region described in the third row covers the first and the second quadrants, and this results in a evaluation of $\mathrm{Re}[e^{j\Theta}]$ with positive or negative sign. Therefore, the lower bound of y is reached with the upper bound of magnitude and upper bound of phase angle, which makes the value of $\cos(\Theta_u)$ the largest negative number. The upper bound of y is obtained in a converse way.

Figure 8 shows the implementation flow of the proposed general-signal transient bound determination method. It starts from a time-domain sampling of input signal $x(t)$ and given system transfer function bounds in frequency domain. The FFT operation transforms the input signal to its spectrum, and then the proposed rules in Table I are applied to determine the magnitude and phase combinations for lower and
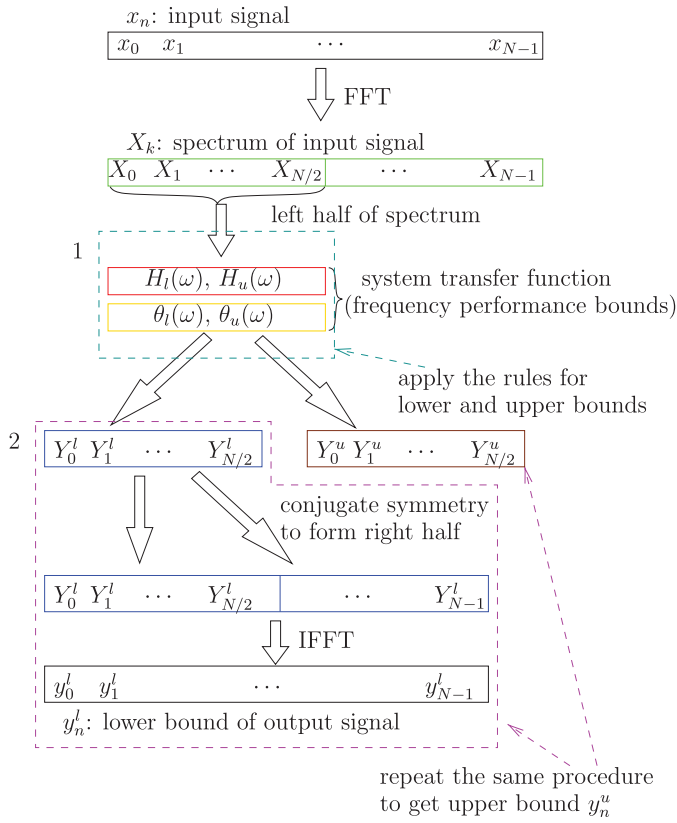
Fig. 8. The proposed general-signal transient bound determination method.

upper time-domain bounds at every frequency point in the left half of the spectrum. This process is marked by the dashed line box, labeled "1" in Figure 8. Next, frequency domain results, that is, $Y_0, Y_1, \ldots, Y_{N/2}$, either lower ones or upper ones, are used to construct a full N-length series based on conjugate symmetry property. Last, IFFT is used to calculate the final result of time-domain bounds. This procedure is also marked by dashed line box, labeled "2" in the figure.

5. NUMERICAL RESULTS

In this section, we show experimental results of the proposed method on some benchmark analog circuit netlists. Both frequency-domain bounds and time-domain bounds are calculated by our new method. As an application, frequency-domain analog yield analysis is also performed for two circuits based on the magnitude and phase bounds. This section is divided into two sections: the first shows the frequency-domain response bound results, while the second one demonstrates those results of time-domain response bounds.

For running time comparisons, we also measure the time cost by the commercial HSPICE, which runs all the Monte Carlo (MC) simulations. All running times are obtained from a Linux server with a 2.4GHz Intel Xeon Quad-Core CPU and 36GB memory.
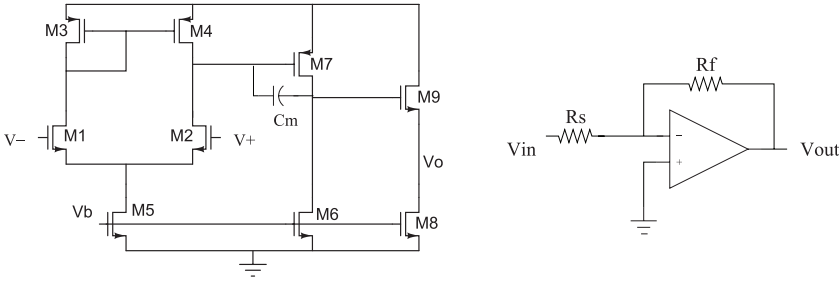
(a) The circuit schematic of the amplifier.

(b) The test circuit using negative feedback on opamp.

Fig. 9.   CMOS operational amplifier and its test circuit.

Table II. Variational Parameters Used in the CMOS Opamp

Affected transistor	Model parameter	Nominal value	Variation
M1, M2	g_{m}	1.48×10^{-5} Ω^{-1}	5%
	g_{ds}	2.33×10^{-8} Ω^{-1}	
	C_{gs}	5.16 fF	
	C_{gd}	0.31 fF	
M9	g_{m}	1.23×10^{-4} Ω^{-1}	10%
	g_{ds}	3.94×10^{-7} Ω^{-1}	

5.1. Frequency-Domain Response Bounds

The exact transfer function expressions are generated by the DDD symbolic analysis tool [Shi and Tan 2000], and all the follow-up optimization-based bound calculations are done in MATLAB. The nonlinear constrained optimizations are solved by the `fmincon` function in MATLAB's Optimization Toolbox [Mathworks 2012]. The active-set algorithm is chosen as the optimization algorithm in `fmincon`. (We have also tried other methods and found that the active-set method is the most robust and reliable.)

We first investigate the accuracy and efficiency of our frequency-domain method with typical circuit examples. Figure 9(a) shows the schematic of a CMOS operational amplifier, which contains nine transistors. Its differential inputs are provided at the gate terminals of the differential pair of M1 and M2, while the output is observed at the output node of the source follower stage. For the purpose of testing and simulation, a feedback loop is added between its output and negative input, and the two resistors R_f and R_s have the same value. Therefore, the circuit shown in Figure 9(b) is configured as a unit-gain buffer, $V_{\mathrm{out}} = -(R_f/Rs)V_{\mathrm{in}} = -V_{\mathrm{in}}$. DC analysis is first performed by HSPICE to obtain the operating point, and then small-signal models of nonlinear devices, such as MOS transistors, are used for DDD symbolic analysis and transfer function evaluation. For example, the original NMOS device is replaced by the equivalent circuit model consisting of voltage-controlled current source (VCCS), gate-source capacitance (C_{gs}), gate-drain capacitance (C_{gd}), terminal resistance, and so on. We actually use the MOS small-signal model shown in Figure 3, with singular network elements, like nullator and norators. The combination of these elements in the MOS model behaves as an ideal VCCS. However, the properties of the nullator (which does not allow current flowing through it and provides zero voltage difference between its two terminals, i.e., the voltage values on nodes G and N are the same) and the norator (which allows any voltage across its two terminals and any current flowing through it) allow us to formulate more compact equations than MNA [Sánchez-López et al. 2011].
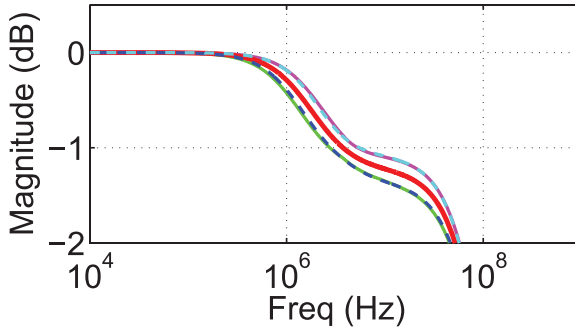
Fig. 10.   Magnitude bounds of CMOS opamp using the proposed method and MC simulations. The thick solid curve is nominal magnitude response, the two thin solid curves are bounds from the proposed method, and dashed curves are 3-sigma bounds of 5,000 times MC analysis. It is obvious that our bounds are tight and accurate if compared with MC bounds.
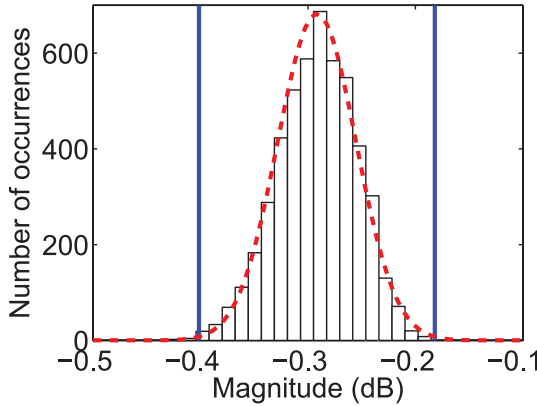

Fig. 11.   The histogram of the magnitude distribution of the CMOS opamp at frequency $f = 1$ MHz using 5,000 times MC simulation. The two vertical lines are the bounds from the proposed method, and the dashed curve is the estimated Gaussian pdf using our bound information.

For the CMOS opamp, we enumerate the variational parameters used in the experiments in Table II. The variational parameters are introduced to transconductance (g_m), resistors, and capacitors inside the transistor model. Since transistors in the differential pair are subjected to symmetry requirements, we apply a relatively small variation (5%) on them. As a result, there are a total of ten variational parameters in this example. The active filter example has seven variational parameters, which are modeled in a similar way. Note that we assume that information of the variational parameters listed in Table II have been characterized during device-level variation modeling process based on the data from foundry. The parameters will take Gaussian distributions with their 3-sigma bounds ($[\mu - 3\sigma, \mu + 3\sigma]$, where μ is the mean and σ is the standard deviation of the Gaussian variable) matching the bounds listed in Table II.

After the symbolic expressions, that is, numerator and denominator, of the opamp's transfer function are obtained, the nominal frequency response can be evaluated straightforwardly using the specified parameter values. The lower and upper bounds of the magnitude and phase are then obtained by the aforementioned constrained optimization. Figure 10 plots the nominal magnitude curve along with its lower and upper bounds. On the same figure, we also plot the 3-sigma bounds calculated from

Table III. Statistical Information of the CMOS
Opamp Circuit

CMOS opamp		
Runtime (seconds)	MC	85.2
	proposed	3.8
Mean value (μ)	MC	−0.29
Unit: dB	proposed	−0.29
Std. value (σ)	MC	0.0365
Unit: dB	proposed	0.0367
Yield rate	MC	93.9%
	proposed	94.5%

Note: Comparison with 5,000 times MC.

Table IV. Statistical Information of the CMOS
Filter

| CMOS Filter		
Runtime (seconds)	MC	100.4
	proposed	8.2
Mean value (μ)	MC	26.83
Unit: dB	proposed	26.81
Std. value (σ)	MC	0.389
Unit: dB	proposed	0.384
Yield rate	MC	82.7%
	proposed	84.2%

Note: Comparison with 5,000 times MC.

5,000 MC samples of the same circuits. It is obvious that our bounds include all possible variations and do not show much over-conservativeness. The result demonstrates the effectiveness of the optimization-based method to find accurate bounds.

We also remark that for a fair comparison, both the MC method and the proposed performance bound analysis method are applied to the same circuits with the same device models and statistical distributions of parameters.

As an application of the proposed method, we apply the proposed method for analog yield estimation. We illustrate this using the same opamp. The yield estimation is calculated using preset specifications. For the CMOS opamp in Figure 9, we set a requirement that the accepted circuit should have its gain larger than −0.35 dB at frequency $f = 1$ MHz. HSPICE MC analysis with 5,000 samples gives the yield as 93.9%, and the histogram of all samples is drawn in Figure 11. Meanwhile, the predicted yield using the proposed method is 94.5%, which is fairly close to that of the MC analysis. The detailed statistics of the comparison are shown in Table III. With the accurate calculation of performance bounds and the yield, the presented method only takes 3.8 seconds. This is a 22× speedup over the 5,000 MC simulations.

The proposed algorithm is also applied to a CMOS active filter [Palma-Rodriguez et al. 2012] (circuit diagram not shown in our article). Figure 12 shows the magnitude bounds together with HSPICE MC results. In this figure, we show the curves of the proposed method, the 3-sigma curves, and 6-sigma curves from MC results. As we can see, the proposed method matches the 3-sigma curves very well. We remark that our parameter variations are mainly bounded by their 3-sigma ranges, which lead to a better match with 3-sigma responses of the MC analysis. The statistical data is listed in Table IV. A speedup of 13× is observed on this example.
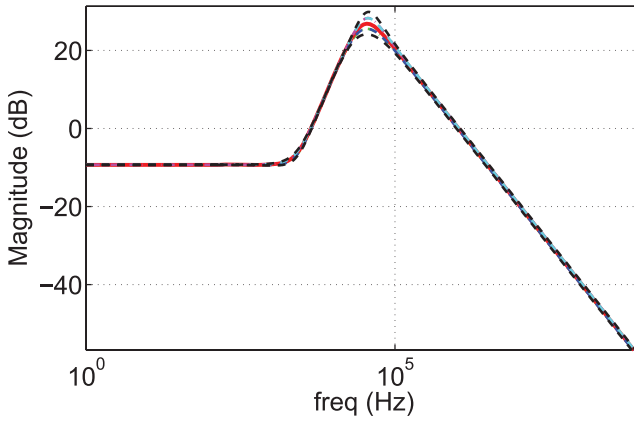
(a) Magnitude response of the active filter on the frequency sweep range. This circuit is more sensitive to variation between 10^4 and 10^5 Hz.
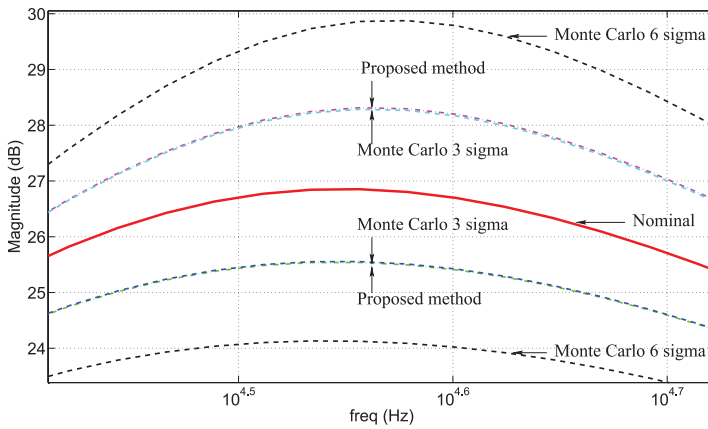

(b) Detailed comparison of magnitude bounds from the proposed method and MC around $10^{4.5}$ Hz. The bounds from our method and the 3-sigma and 6-sigma bounds of MC samples are properly annotated in the figure.

Fig. 12. Comparison of bounds from MC and the proposed method of magnitude response of active filter. The MC bounds are calculated as 3-sigma and 6-sigma bounds of 5,000 samples. It is noticeable that our bounds capture MC's 3-sigma bounds accurately.

Table V. Performance Comparison of TIDBA against MC Method (10,000 Times)

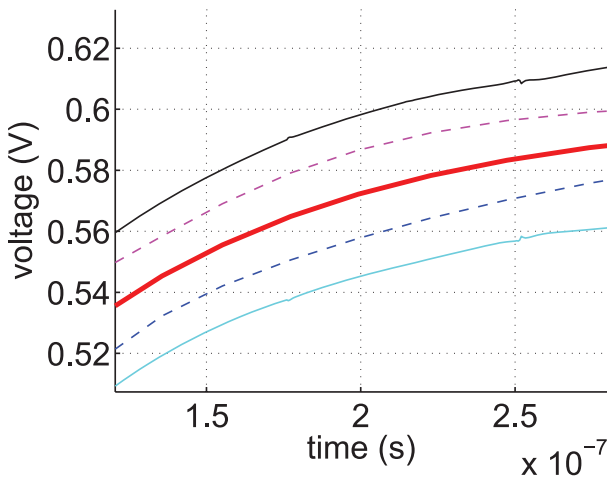| Circuit name	CPU time		speed up
	MC (10,000)	TIDBA	
Opamp	362.9 s	11.2 s	32×
Filter	459.7 s	12.1 s	38×
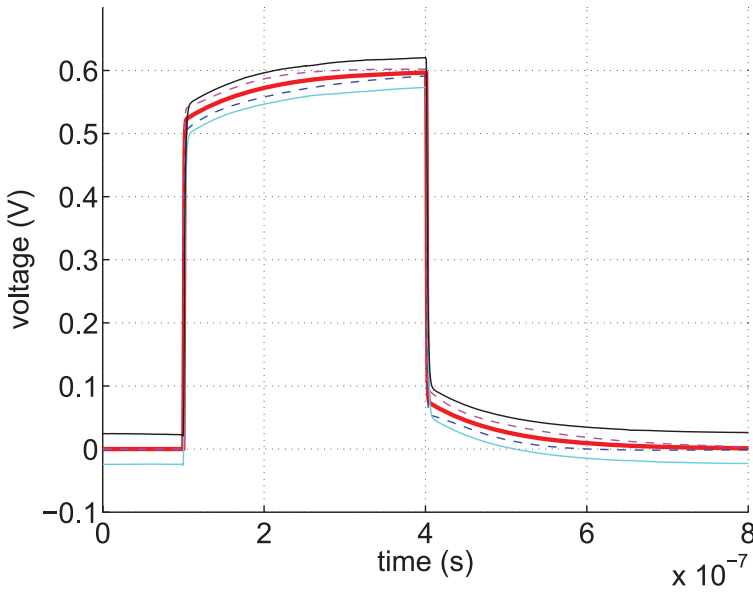
(a) The whole plot.



(b) Detailed view around $t = 2 \times 10^{-7}$ s.

Fig. 13.   Time-domain response of CMOS opamp with pulse input. Thick solid curve represent the nominal response. Thin solid curves are bounds from the proposed TIDBA method, while dash curves are bounds of 10,000 MC results.
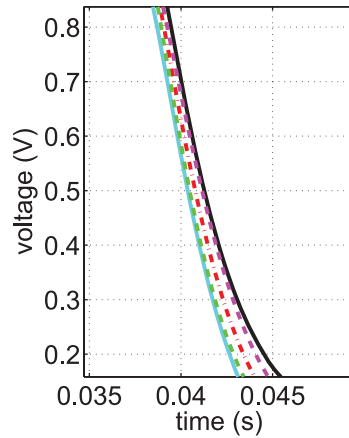
5.2. Time-Domain Response Bounds

Using the frequency-domain bounds we calculated in the previous experiments, the time-domain bounds of the CMOS opamp are obtained by the TIDBA method. Figure 13
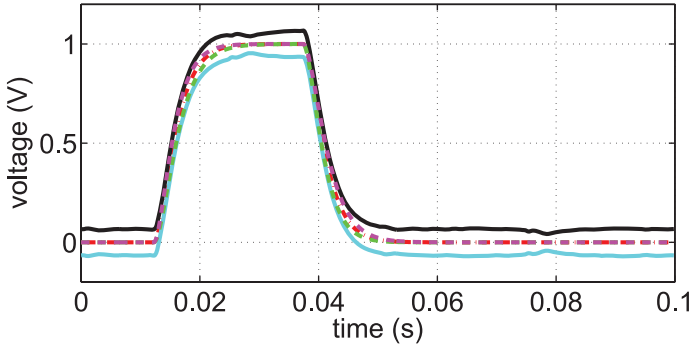
(a) The whole plot.
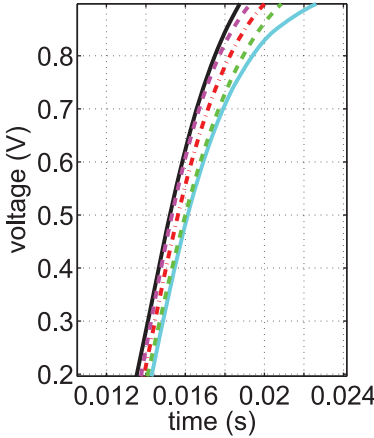
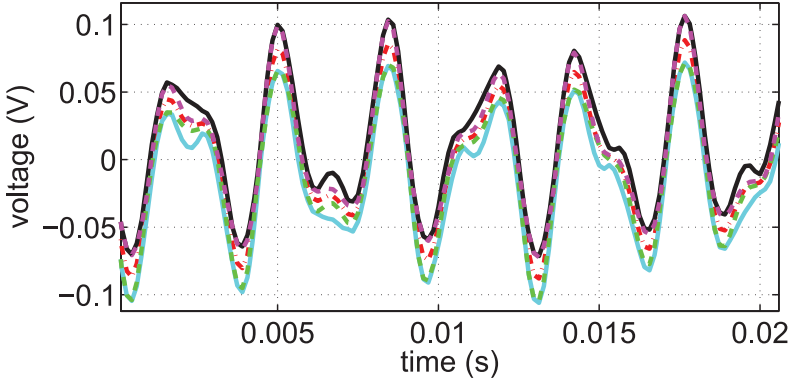

(b) Detail of up ramp.

(c) Detail of down ramp.

Fig. 14.   Time-domain response of the active filter with pulse wave input. The two solid curves are the lower and upper bounds from the proposed TIDBA method, and the dashed curves are bounds of 10,000 MC simulations. The dot-dashed curve in the middle is the nominal transient response.

shows bounds of 10,000 MC pulse responses at the output node of the opamp as dashed curves, and the bounds generated from TIDBA are overlaid onto the same figure as solid curves.

We also simulated the active filter with a pulse waveform as input. Bounds of MC waveforms observed at the output node are plotted as dashed curves in Figure 14. Due to the process variation of the filter, it can be observed that the output waveforms deviated from its nominal benchmark. Detailed plots of the up ramp and down ramp are shown in Figures 14(b) and 14(c). The time-domain performance bounds, computed by TIDBA, are plotted as solid curves. An input signal comprised of several sinusoidal waves are also used to test this filter. Its possible minimum and maximum values in time domain and the TIDBA bounds are plotted in Figure 15.

We notice that the bounds given by TIDBA may not be able to converge to the steady state of the response, for example, after 0.06 seconds in Figure 14(a), which should
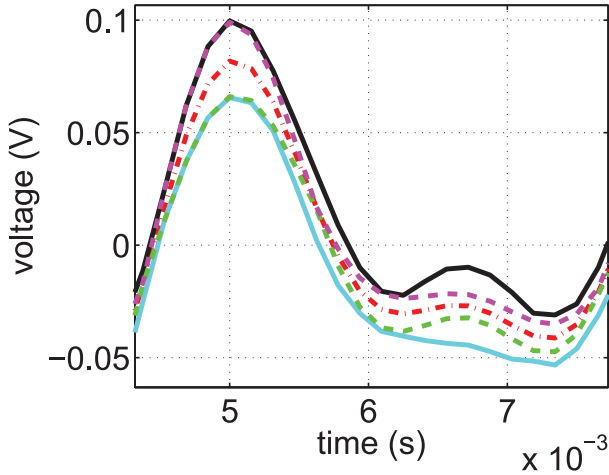
(a) The whole plot.

(b) Detailed view around $t = 6 \times 10^{-3}$ s.

Fig. 15.   Time-domain response of the active filter with sinusoidal wave input. The two solid curves are the lower and upper bounds from the proposed method, while the dashed curves are bounds of 10,000 MC simulations. The dot-dashed curve in the middle is the nominal response.

be zero. This is due to the loss of dependence between magnitude and phase when we apply the frequency response bounds of inequalities (3) and (4). However, for many steady states, which are known to be zero, even with variations in parameters, we can ignore the bounds given by the proposed method. Another way to mitigate this problem is to directly compute time-domain bounds using the optimization-based approaches, which will be investigated in our future works.

We remark that TIDBA seemingly overestimates the performance bounds, as shown in Figures 13 to 15. But the results at least are conservative. The overestimation is due to the nature of the proposed algorithm, as we formulate the problem into two phases. In the first phase, performance bounds are computed in frequency domain for

magnitudes and phases independently. The second phase computes the time-domain bounds based on the frequency-domain bounds. Such a two-phase approach relaxes some properties of the signals going through analog systems in the time domain. For instance, we lose the dependence between magnitudes and phases as we optimize them separately. As a result, the two-phase method leads to a relaxed optimization problem and thus overestimated results.

Table V summarizes the experiment parameters and running time comparisons. The two examples still use the same variational parameter setup as in the frequency domain experiments, and the MC transient simulation generates 10,000 samples. TIDBA takes a total number of 6,400 time-domain samplings on input stimulus and feeds them to FFT. The running time measurements of MC and TIDBA are also listed in the table. The maximum speedup of TIDBA over MC could be 38×.

6. CONCLUSIONS AND FUTURE WORKS

We have proposed a new performance bound analysis flow of analog circuits considering process variations in both time and frequency domains. The new method applies a graph-based analysis technique to derive the symbolic transfer functions of linear(ized) analog circuits. Then the problem of finding frequency response bounds is formulated into a nonlinear constrained optimization problem, where the cost functions are magnitude and phase of the transfer function subject to the linear constraints, which are the upper and lower bounds of process variational parameters. The frequency-domain bounds calculated in this way are accurate and show no over-conservativeness suffered by the previous approaches. Based on the frequency response bounds, we further propose an algorithm to compute time-domain response bounds of circuits with any arbitrary input signals. Experimental results from several analog benchmark circuits show that the proposed method gives the correct bounds verified by Monte Carlo (MC) analysis while it delivers one order of magnitude speedup over MC in both frequency and time domain. We have also shown analog circuit yield analysis as an application of the frequency-domain variational bound analysis.

Currently, the proposed method can only work on linear or linearized analog circuits. We are working on the performance bound analysis for general nonlinear circuits. For many circuits where time domain analysis is mainly performed, direct time-domain-based bound analysis using optimization method will be more desirable and will be investigated in the future.

REFERENCES

BYRD, R. H., SCHNABEL, R. B., AND SHULTZ, G. A. 1987. A trust region algorithm for nonlinearly constrained optimization. *SIAM J. Numer. Anal. 24,* 5, 1152–1170.

FLOUDAS, C. A. 1995. *Nonlinear and Mixed-Integer Optimization: Fundamentals and Applications (Topics in Chemical Engineering)*. Oxford University Press.

FRIGO, M. AND JOHNSON, S. G. 2013. The halfcomplex-format DFT in FFTW. Tech. rep., MIT. http://www.fftw.org/doc/The-Halfcomplex_002dformat-DFT.html.

GILL, P. E., MURRAY, W., MICHAEL, AND SAUNDERS, M. A. 1997. SNOPT: An SQP algorithm for large-scale constrained optimization. *SIAM J. Optim. 12,* 979–1006.

HAO, Z., SHEN, R., TAN, S. X.-D., AND SHI, G. 2011. Performance bound analysis of analog circuits considering process variations. In *Proceedings of the Design Automation Conference (DAC)*. 310–315.

KHARITONOV, V. L. 1978. Asymptotic stability of an equilibrium position of a family of systems of linear differential equations. *Differential. Uravnen. 14*, 2086–2088.

KIM, J., JONES, K., AND HOROWITZ, M. 2007. Fast, non-Monte-Carlo estimation of transient performance variation due to device mismatch. In *Proceedings of the IEEE/ACM Design Automation Conference (DAC)*.

KOLEV, L., MLADENOV, V., AND VLADOV, S. 1988. Interval mathematics algorithms for tolerance analysis. *IEEE Trans. Circ. Syst. 35,* 8, 967–975.

LATHI, B. P. 1998. *Modern Digital and Analog Communication Systems* 3rd Ed. Oxford University Press.

LIU, B., MESSAOUDI, J., AND GIELEN, G. 2012. A fast analog circuit yield estimation method for medium and high dimensional problems. In *Proceedings of the Design, Automation, and Test in Europe (DATE)*. 751–756.

MASUDA, H., OHKAWA, S., KUROKAWA, A., AND AOKI, M. 2005. Challenge: Variability characterization and modeling for 65- to 90-nm processes. In *Proceedings of the IEEE Custom Integrated Circuits Conference*.

MATHWORKS 2012. MATLAB Optimization Toolbox. http://www.mathworks.com/help/toolbox/optim/.

NASSIF, S. 2007. Model to hardware correlation for nm-scale technologies. In *Proceedings of the IEEE International Workshop on Behavioral Modeling and Simulation (BMAS)*. Keynote speech.

OPPENHEIM, A. V. AND SCHAFER, R. W. 1999. *Discrete-Time Signal Processing*. Prentice Hall, Upper Saddle River, NJ.

PALMA-RODRIGUEZ, A. A., TLELO-CUAUTLE, E., RODRIGUEZ-CHAVEZ, S., AND TAN, S. X.-D. 2012. DDD-based symbolic sensitivity analysis of active filters. In *Proceedings of the International Caribbean Conference on Circuits, Devices, and Systems (ICCDCS)*. 170–173.

PELGROM, M., DUINMAIJER, A., AND WELBERS, A. 1989. Matching properties of mos transistors. *IEEE J. Solid State Cir.*

PRITCHARD, C. AND WIGDOROWITZ, B. 1997. Improved method of determining time-domain transient performance bounds from frequency response uncertainty regions. *Int. J. Control 66,* 2, 311–327.

QIAN, L., ZHOU, D., WANG, S., AND ZENG, X. 2010. Worst case analysis of linear analog circuit performance based on Kharitonov's rectangle. In *Proceedings of the IEEE International Conference on Solid-State and Integrated Circuit Technology (ICSICT)*.

RUTENBAR, R. 2007. Next-generation design and EDA challenges. In *Proceedings of the Asia South Pacific Design Automation Conference (ASPDAC)*. Keynote speech.

SAIBUA, S., QIAN, L., AND ZHOU, D. 2011. Worst case analysis for evaluating VLSI circuit performance bounds using an optimization method. In *Proceedings of the IEEE/IFIP 19th International Conference on VLSI and System-on-Chip*. 102–105.

SÁNCHEZ-LÓPEZ, C., FERNÁNDEZ, F. V., TLELO-CUAUTLE, E., AND TAN, S. X.-D. 2011. Pathological element-based active device models and their application to symbolic analysis. *IEEE Trans. Circ. Syst. 58,* 6, 1382–1395.

SHI, C.-J. AND TAN, X.-D. 2000. Canonical symbolic analysis of large analog circuits with determinant decision diagrams. *IEEE Trans. Comput.-Aid. Des. Integr. Circ. Syst. 19,* 1, 1–18.

SHI, C.-J. AND TAN, X.-D. 2001. Compact representation and efficient generation of s-expanded symbolic network functions for computer-aided analog circuit design. *IEEE Trans. Comput.-Aid. Des. Integr. Circ. Syst. 20,* 7, 813–827.

SHI, C.-J. R. AND TIAN, M. W. 1999. Simulation and sensitivity of linear analog circuits under parameter variations by robust interval analysis. *ACM Trans. Des. Autom. Electron. Syst. 4*, 280–312.

SINGHEE, A. AND RUTENBAR, R. A. 2010. Why quasi-Monte Carlo is better than Monte Carlo or latin hypercube sampling for statistical circuit analysis. *IEEE Trans. Comput.-Aid. Des. Integr. Circ. Syst. 29,* 11, 1763–1776.

SONG, Y., YU, H., DINAKARRAO, S. M. P., AND SHI, G. 2013. SRAM dynamic stability verification by reachability analysis with consideration of threshold voltage variation. In *Proceedings of the International Symposium on Physical Design (ISPD)*. 43–49.

SPENCE, R. AND SOIN, R. 1988. *Tolerance Design of Electronic Circuits*. Addison-Wesley, Reading, MA.

TAN, S. X.-D., GUO, W., AND QI, Z. 2005. Hierarchical approach to exact symbolic analysis of large analog circuits. *IEEE Trans. Comput.-Aid. Des. Integr. Circ. Syst. 24,* 8, 1241–1250.

TIAN, W., LING, X.-T., AND LIU, R.-W. 1996. Novel methods for circuit worst-case tolerance analysis. *IEEE Trans. Circ. Sys. I: Fund. Theory Appl. 43,* 4, 272–278.

VLACH, J. AND SINGHAL, K. 1995. *Computer Methods for Circuit Analysis and Design*. Van Nostrand Reinhold, New York, NY.